APL Materials

γ-phase inclusions as common structural defects in alloyed β-$(Al_xGa_{1-x})_2O_3$ and doped β-Ga_2O_3 films

Cite as: APL Mater. **9**, 051119 (2021); https://doi.org/10.1063/5.0038861
Submitted: 27 November 2020 . Accepted: 28 April 2021 . Published Online: 17 May 2021

Celesta S. Chang, Nicholas Tanen, Vladimir Protasenko, Thaddeus J. Asel, Shin Mou, Huili Grace Xing, Debdeep Jena, and David A. Muller

γ-phase inclusions as common structural defects in alloyed β-$(Al_xGa_{1-x})_2O_3$ and doped β-Ga_2O_3 films

Cite as: APL Mater. 9, 051119 (2021); doi: 10.1063/5.0038861
Submitted: 27 November 2020 • Accepted: 28 April 2021 •
Published Online: 17 May 2021

View Online Export Citation CrossMark

Celesta S. Chang,[1,2,a] Nicholas Tanen,[3] Vladimir Protasenko,[4] Thaddeus J. Asel,[5] Shin Mou,[5] Huili Grace Xing,[3,4,6] Debdeep Jena,[3,4,6] and David A. Muller[2,6,b]

AFFILIATIONS

[1] Department of Physics, Cornell University, Ithaca, New York 14853, USA
[2] School of Applied and Engineering Physics, Cornell University, Ithaca, New York 14853, USA
[3] Department of Materials Science and Engineering, Cornell University, Ithaca, New York 14853, USA
[4] School of Electrical and Computer Engineering, Cornell University, Ithaca, New York 14853, USA
[5] Air Force Research Laboratory, Materials and Manufacturing Directorate, Wright Patterson AFB, Ohio 45433, USA
[6] Kavli Institute at Cornell for Nanoscale Science, Cornell University, Ithaca, New York 14853, USA

[a] **Present address:** Research Laboratory of Electronics, Massachusetts Institute of Technology, Cambridge Massachusetts 02139, USA
[b] **Author to whom correspondence should be addressed:** dm24@cornell.edu

ABSTRACT

β-Ga_2O_3 is a promising ultra-wide bandgap semiconductor whose properties can be further enhanced by alloying with Al. Here, using atomic-resolution scanning transmission electron microscopy, we find the thermodynamically unstable γ-phase is a ubiquitous structural defect in both β-$(Al_xGa_{1-x})_2O_3$ films and doped β-Ga_2O_3 films grown by molecular beam epitaxy. For undoped β-$(Al_xGa_{1-x})_2O_3$ films, we observe γ-phase inclusions between nucleating islands of the β-phase at lower growth temperatures (~500–600 °C). In doped β-Ga_2O_3, a thin layer of the γ-phase is observed on the surfaces of films grown with a wide range of n-type dopants and dopant concentrations. The thickness of the γ-phase layer was most strongly correlated with the growth temperature, peaking at about 600 °C. Ga interstitials are observed in the β-phase, especially near the interface with the γ-phase. By imaging the same region of the surface of a Sn-doped β-$(Al_xGa_{1-x})_2O_3$ after *ex situ* heating up to 400 °C, a γ-phase region is observed to grow above the initial surface, accompanied by a decrease in Ga interstitials in the β-phase. This suggests that the diffusion of Ga interstitials toward the surface is likely the mechanism for growth of the surface γ-phase and more generally that the more-open γ-phase may offer diffusion pathways to be a kinetically favored and early forming phase in the growth of Ga_2O_3. However, more modeling and simulation of the γ-phase and the interstitials are needed to understand the energetics and kinetics, the impact on electronic properties, and how to control them.

INTRODUCTION

Ga_2O_3 is known to have at least five different phases, with formation energies ordered as $\beta(C2/m) < \kappa(Pna2_1) < \alpha(R\bar{3}c) < \delta(Ia\bar{3}) < \gamma(Fd\bar{3}m)$ at temperatures below 1600 K.[1,2] Among these, β-Ga_2O_3 has received a primary focus on the power electronics community for its thermodynamic stability.[1–3] Due to its ultra-wide bandgap (4.4–4.9 eV) and availability of high-quality melt-grown substrates including semi-insulating to heavily n-type doped wafers, early demonstrations of both lateral and vertical devices with breakdown voltages as high as 3 kV were achieved.[4–11]

On the other hand, being the least stable phase in the Ga_2O_3 family, far less is known about γ-Ga_2O_3 and studies have been relatively limited. Owing to its mesoporous crystal structure, γ-Ga_2O_3 has been studied as a catalyst when grown in nanorods.[12] Epitaxial thin films have been grown on substrates such as MgO or sapphire,

where dopants are known to provide phase stability.[5,13,14] In fact, γ-Ga_2O_3 (space group $Fd\bar{3}m$) has a cubic defective spinel structure with two cation vacancies in the primitive unit cell.[15–17] 14 Ga vacancy configurations were considered in a first-principles study, but they concluded that there was no specific site preference.[1] Consequently, we assume that the vacancies are uniformly distributed and use the perfect spinel with a uniformly reducted Ga-site occupancy. This unique structure can provide a platform for developing new functionalities that can arise by heteroepitaxial growth on spinel oxides. The direct and indirect energy bandgaps of γ-Ga_2O_3 are E_g = 5.0 eV and 4.4 eV, respectively,[14] slightly higher than those of β-Ga_2O_3 (E_g = 4.4–4.9 eV). Bandgap engineering by the growth of γ-$(Al_xGa_{1-x})_2O_3$ has been reported to achieve bandgaps up to ~6.3 eV (x = 0.67) by Oshima *et al.*,[18] suggesting its potential as a future generation ultra-wide bandgap semiconductor.

Unlike traditional semiconductor materials such as Si, Ge, and diamond (C)[19] and wurtzite (III-N)[20] and zincblende (GaAs)[21] structures, which are known to be significantly more stable thermodynamically than their polymorphs, metastable phases of Ga_2O_3 are relatively close to β-Ga_2O_3 in the phase diagram. As a result, many studies have reported the coexistence of two or more phases arising during the growth of thin film Ga_2O_3.[22–26] A recent study also reported the possible formation of γ-$(Al_xGa_{1-x})_2O_3$ in metal organic chemical vapor deposition (MOCVD) grown β-$(Al_xGa_{1-x})_2O_3$ at Al concentrations of $27\% < x < 40\%$,[26] although an alternate interpretation of their TEM image showing γ-$(Al_xGa_{1-x})_2O_3$ in terms of stacking faults in the β-phase has also been made.[27–29] In this study, we observe γ-Ga_2O_3 inclusions as a common structural defect that is broadly found in a series of doped β-Ga_2O_3 and β-$(Al_xGa_{1-x})_2O_3$, at compositions of interest for improved device performance and higher breakdown voltages.

Because β-Ga_2O_3 is used for power electronic applications, the observation of the γ-phase poses an interesting question as to its potential impact on the progress in this field. γ-phase inclusions in the β-phase structure could be detrimental for device performance. The γ-phase at the surface of doped films can lead to non-ideal high current ohmic contact regions, while γ-$(Al_xGa_{1-x})_2O_3$ in β-$(Al_xGa_{1-x})_2O_3$ could severely compromise the gate switching behaviors under high-field. Additionally, as large voltages and currents used in power electronics can lead to significant Joule heating of devices without proper thermal management, device reliability can be harmed by Ga_2O_3 polymorphs that could be transformed at elevated temperatures. More understanding of γ-Ga_2O_3 is needed to measure the extent to which it can affect the device performance and to prevent its unintentional formation in β-Ga_2O_3.

In this paper, we use molecular beam epitaxy (MBE) to grow crystalline thin films of Ge- and Si-doped β-Ga_2O_3, Sn-doped β-$(Al_{0.15}Ga_{0.85})_2O_3$, and an undoped series of β-$(Al_xGa_{1-x})_2O_3$. Since MBE growth occurs in ultrahigh vacuum systems using high purity source materials, it allows for high purity, highly crystalline thin films with atomically smooth and abrupt interfaces, which are necessary for high performance electronic devices. We then characterize the films using atomic force microscopy (AFM), high resolution x-ray diffraction (HRXRD), and scanning transmission electron microscopy (STEM). Here, we find that γ-Ga_2O_3 is present at the surfaces of doped β-Ga_2O_3, while γ-$(Al_xGa_{1-x})_2O_3$ in β-$(Al_xGa_{1-x})_2O_3$ is also found as inclusions inside the film at low growth temperatures. Expanding the phase space studied in Ref. 26, here, we report that even at relatively low Al concentrations (<20%), the inclusion of γ-$(Al_xGa_{1-x})_2O_3$ can be observed, and therefore, it appears that the formation of γ-$(Al_xGa_{1-x})_2O_3$ is also sensitive to growth conditions rather than solely to the Al composition. We suggest that the γ-phase inclusions, especially near the surface, may be stabilized by the presence of dopants during growth. In the section titled Correlation of Ga interstitials to the formation of γ-Ga_2O_3, we focus on the Ga-interstitials that are frequently observed near the formation of the γ-phase in both alloyed and doped β-phase films. From our *ex situ* heating results, we suggest the possibility of Ga interstitials participating in the formation of the γ-phase by out-diffusion, which suggests a mechanism for why the thermodynamically unstable γ-phase could be a kinetically preferred phase, especially for the lower-temperature growth of Ga_2O_3.

METHODS

In this work, we describe a set of eight samples grown by plasma assisted MBE (PAMBE). Specific growth parameters for each of the samples and sample labels can be found in Table I. Two Ge-doped β-Ga_2O_3 thin films (DG1 and DG3) were grown using a Veeco GEN Xcel PAMBE system in Air Force Research Laboratory (AFRL), equipped with standard effusion cells for Ge and Ga and an unibulb RF plasma source for oxygen. The films were grown with substrate temperatures of 550 and 650 °C and an oxygen flow rate of 1.55 SCCM, which resulted in a background pressure of 1.5×10^{-5} Torr and 300 W of oxygen plasma power. Ge was maintained at 600 °C for all growths, and the Ga beam equivalent pressure was 6.0×10^{-8} Torr, which is in the O-rich regime for our system.

Ge-doped β-Ga_2O_3 (600 °C, DG2), Si-doped β-Ga_2O_3 (DSi), and a series of β-$(Al_xGa_{1-x})_2O_3$ films (A1–A3) were grown using a Veeco Gen930 MBE system at Cornell University. Reflection high-energy electron diffraction (RHEED) patterns are provided in Fig. S1 to show the film quality. The activated oxygen flux was provided using a Veeco RF plasma source. Al and Ga metals were provided using standard Veeco effusion cells. The films were all grown on edge-defined film-fed grown (EFG) (010) substrates purchased from Novel Crystal Technology (NCT), which were diced into 5×5 mm^2 pieces and In-mounted on a two-inch silicon carrier wafer. Prior to growth, the substrates were cleaned using a degreasing soap and deionized water followed by sonication in acetone, methanol, isopropyl alcohol, and again deionized water. The films were annealed for 30 min at 800 °C (as measured by a thermocouple) while being exposed to an oxygen plasma prior to growth to descum the growth surface. The Si- and Ge-doped (600 °C) samples were prepared in a similar way; however, no plasma descum was performed for these two samples. For the Sn-doped sample (DSn), purchased from NCT, effusion cells were used to provide Ga, Al, and SnO_2. In order to obtain precise Al and Sn concentrations, calibration samples were grown. The Al concentration was determined using Rutherford back scattering (RBS), and the Sn concentration was determined using electrochemical capacitance voltage (ECV) measurements to profile N_d–N_a vs depth.

The β-$(Al_xGa_{1-x})_2O_3$ films in this experiment were grown at 500, 600, and 700 °C (as measured by the MBE CAR thermocouple). The alloyed samples are also labeled A1–A3 with ascending growth temperature. Samples A2 and A3 were grown using

TABLE I. Summary of the growth conditions for doped and undoped β-$(Al_xGa_{1-x})_2O_3$ samples discussed in this study. DG1 and DG3 were grown using a Veeco GEN Xcel PAMBE system in AFRL, DSn by NCT, while the other samples were grown in a Veeco Gen930 MBE system at Cornell university. The growth rate was extracted from SIMS for DG1 and DG3 and from XRD for all other samples.

Sample label	Sample	T_{sub} (°C)	Ga BEP (Torr)	Al BEP (Torr)	O_2 (flow, SCCM/RF power, W/P_{GM}, Torr)	Growth rate (nm/h)	Film thickness (nm)	Al% from XRD	Doping density	AFM 2 × 2 μm^2 rms (nm)	Grower
DG1	Ge–Ga_2O_3	550	6.00×10^{-8}	N/A	$1.55/300/1.50 \times 10^{-5}$	48.5	400	N/A	5×10^{18}	0.71	AFRL
DG2	Ge–Ga_2O_3	600	2.05×10^{-8}	N/A	$0.57/250/1.00 \times 10^{-5}$	38	152(doped)/152(UID)	N/A	N/A	0.80	Cornell
DG3	Ge–Ga_2O_3	650	6.00×10^{-8}	N/A	$1.55/300/1.50 \times 10^{-5}$	50.5	400	N/A	$\sim 10^{17}$	1.51	AFRL
DSn	Sn–$(Al_{0.15}Ga_{0.85})_2O_3$	550	770 °C (cell T)	876 °C (cell T)	3 SCCM O_3 flow rate/SnO_2 750 °C cell T	167	20(doped)/5(UID)/ 300(UID Ga_2O_3)	15 (from RBS)	2×10^{18}	0.50	NCT
DSi	Si–Ga_2O_3	650	3.10×10^{-8}	N/A	$1.40/250/2.28 \times 10^{-5}$	86.5	173(doped)/173(UID)	N/A	2×10^{20}	0.47	Cornell
A1	$(Al_{0.12}Ga_{0.88})_2O_3$	500	5.00×10^{-9}	1.00×10^{-9}	$0.57/250/1.00 \times 10^{-5}$	32	32/16(UID Ga_2O_3)	12.0	N/A	0.34	Cornell
A2	$(Al_{0.16}Ga_{0.84})_2O_3$	600	2.06×10^{-8}	3.84×10^{-9}	$0.57/250/9.52 \times 10^{-6}$	55	55/27(UID Ga_2O_3)	15.5	N/A	0.91	Cornell
A3	$(Al_{0.19}Ga_{0.81})_2O_3$	700	2.06×10^{-8}	3.84×10^{-9}	$0.57/250/9.53 \times 10^{-6}$	38	37/18(UID Ga_2O_3)	19.2	N/A	0.79	Cornell

a Ga beam equivalent pressure (BEP) of 2×10^{-8} Torr (flux of 5.83×10^{13} atoms/cm^2 s) and an Al BEP of 3.5×10^{-9} Torr ($8.04–8.75 \times 10^{12}$ atoms/cm^2 s) in order to provide ~15% Al based on total metal fluxes. The oxygen flow rate of 0.57 SCCM resulted in a chamber pressure of 1×10^{-5} Torr, and the RF forward power for the plasma supply was set to 250 W. We chose the Ga flux, which maximized the growth rate in our system and should correspond to approximately the stoichiometric point, as described by Vogt and Bierwagen.[30]

It should be noted that these β-$(Al_xGa_{1-x})_2O_3$ films were grown at relatively low growth rates (32–55 nm/h) for (010) β-Ga_2O_3 films grown by PAMBE. In comparison, other PAMBE studies typically report growth rates between 120 and 180 nm/h,[31,32] and over 600 nm/h was reported for ozone-MBE,[33] while a growth rate of 1.6 μm/h was recently achieved for suboxide-MBE.[34] Growth rates of almost 20 μm/h and 0.82–1.47 μm/h can be achieved using higher pressure deposition techniques such as halide vapor phase epitaxy (HVPE)[35] and MOCVD,[26] respectively. The low growth rate in our study was a consequence of our oxygen plasma source and system vacuum pumping capacity, which sets an upper limit on the supplied, activated oxygen, and thus the achievable growth rates.

HRXRD measurements were performed on a Panalytical X'pert Pro x-ray diffractometer to obtain film thicknesses and Al concentrations. To study surface morphology, AFM measurements were performed on a Veeco Icon system. Table I also summarizes the Al content extracted from XRD measurements and the AFM root mean square (rms) roughness for the samples discussed in this paper.

Cross-sectional TEM specimens were prepared using a FEI Strata 400 Focused Ion Beam (FIB) and Helios G4-UX FIB with a final milling step of 5 keV to reduce damage. To prevent surface damage from the ion-beam, carbon and platinum protective layers were deposited prior to milling. The samples were then examined by high-angle annular dark field scanning transmission electron microscopy (HAADF-STEM) imaging, using an aberration-corrected Titan Themis operating at 300 keV.

To investigate the relevance of Ga interstitials to γ-phase formation, three Sn-doped β-$(Al_{0.15}Ga_{0.85})_2O_3$ TEM lamellae were heated twice from room temperature up to 200 °C then 400 °C in an argon environment using Thermocraft XST-2-0-12-1V2-F04. A ramping rate of 5 °C/min was used, and the highest temperature was maintained for 2 h. Cooling was let to happen naturally until it reached room temperature, which approximately corresponds to a cooling rate of 30 °C/min.

RESULTS AND DISCUSSIONS

Distinguishing the crystal structure between γ-Ga_2O_3 and superimposed β-Ga_2O_3

Determining the crystal phase simply based on the atomic arrangement seen in STEM images can be difficult and sometimes misleading if the image resolution is too low to distinguish between similar crystal structures. In a previous study by Bhuiyan *et al.*,[26] they reported the presence of γ-$(Al_xGa_{1-x})_2O_3$ with x-ray diffraction as well as STEM imaging. However, a comment by Wouters *et al.*[27] argued that their STEM images instead showed a superimposed crystal structure created by stacking faults of β-$(Al_xGa_{1-x})_2O_3$ that is superficially similar to the γ-phase. The discussion on distinguishing

the two different structures in the comment and the response was made based on the atomic site intensities and image simulations, which were compared with a low signal-to-noise high-angle annular dark field (HAADF)-STEM image.[26–29]

Here, we show that by using an aberration-corrected microscope in a low-noise environment with a combination of imaging modes, we can obtain high-resolution, high signal-to-noise images that eliminate any ambiguity in determining the crystal phases. In HAADF-STEM, the atomic-number (Z) sensitivity roughly scales as $Z^{1.7}$, so heavy Ga atoms show up in the image, while light oxygen is difficult to see.[36] On the other hand, annular bright field (ABF)-STEM imaging has a weaker dependence on the atomic number ($\sim Z^{0.8}$); thus, it can easily capture oxygen sublattices in the presence of relatively heavy Ga atoms.[37] Combining these two imaging modes, we can construct a full crystal structure enabling an easier determination of crystal phases. Figure 1 shows the crystal structures for β-Ga_2O_3 and γ-Ga_2O_3 in different crystallographic zones. The crystal model for β-Ga_2O_3 was constructed based on Ref. 38, while the Fe_3O_4 structure[39] was used for γ-Ga_2O_3 as they are in the same space group.[40] Thus, the crystal model for γ-Ga_2O_3 in Fig. 1(c) assumes that the cation vacancies are distributed uniformly and reflected in an equally reduced occupancy for all Ga sites.[1] Furthermore, we are assuming a projection of several unit cells along the viewing direction, similar to an actual TEM image as in Fig. 1(d). Different colors are used in the crystal model to distinguish the octahedral Ga sites (yellow) from tetrahedral Ga sites (blue).

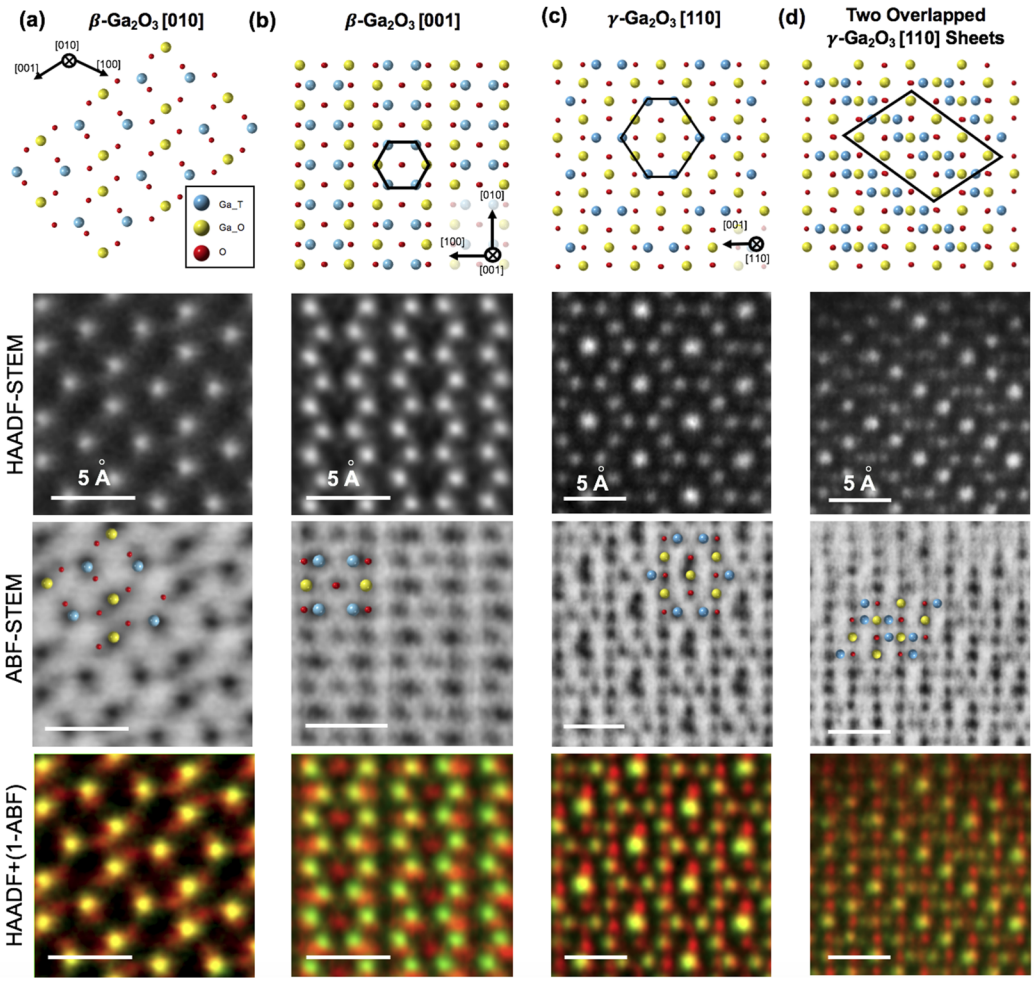

FIG. 1. Crystal structures of β- and γ-phases in different crystal zones. (a) Crystal structure of β-Ga_2O_3 in the [010] crystal zone. The blue atoms and yellow atoms correspond to the tetrahedral Ga *T* and octahedral Ga *O* sites, respectively. (b) Crystal structure of β-Ga_2O_3 in the [001] crystal zone. It forms a hexagonal crystal structure consisting of four tetrahedral sites and two octahedral sites. (c) γ-Ga_2O_3 structure in the [110] crystal zone. The projection of Ga atoms again resembles a hexagonal pattern as in (b); instead, it now has four tetrahedral sites and six octahedral sites in the bigger hexagon, with one of the octahedral sites sitting in the middle of the hexagon. (d) Superimposed crystal structure of two misaligned [110] γ-Ga_2O_3 creating a ladder-like lattice structure. Below, the model structures are the HAADF and ABF STEM images for each of these zone axes. The HAADF contrast is dominated by, and brightest on, the Ga sites. The ABF contrast is opposite, darkest on the Ga sites, but also shows the oxygen sites. On the bottom row are false color overlays of the HAADF in the green channel and the ABF image with contrast inverted in the red channel. The false color map thus reveals the full crystal structure, with oxygen atoms as red and Ga as green.

Simultaneously acquired HAADF-STEM and ABF-STEM images of Sn-doped β-$(Al_{0.15}Ga_{0.85})_2O_3$ and a combined false-color overlay of the two are shown for each crystal structure. The combined image is obtained by color-coding the HAADF image showing Ga atoms in green and the ABF image showing O atoms in red by overlaying the HAADF-STEM image on an inverted ABF-STEM image.

β-Ga_2O_3 with the space group C2/m has lattice parameters of a = 12.214 Å, b = 3.037 Å, and c = 5.798 Å.[41] β-Ga_2O_3 is generally grown parallel to the (010) surface as in Fig. 1(a) because the symmetry of the growth surface prevents twin formation and the growth rate is much faster than that for other substrate orientations in similar MBE growth conditions.[41–43] Observation along the crystal zone of [001] in Fig. 1(b) shows the outlined hexagonal crystal structure, where Ga occupies four tetrahedral sites and two octahedral sites. In contrast, γ-Ga_2O_3 has a defective cubic spinel structure with the space group $Fd\bar{3}m$, as shown in Fig. 1(c). It has a cubic lattice parameter of a = 8.23 Å,[15,16] approximately three times larger in volume and 7% lower in atomic density compared to the β-phase.[40,44] γ-Ga_2O_3 has six tetrahedral Ga sites and five octahedral Ga sites inside a hexagonal structure overlaid in Fig. 1(c). Our observations in the section titled Doped β-Ga_2O_3 will show that the γ-phase tends to grow on the surface of β-(010), starting from the two tetrahedral sites in the small hexagonal structure of β-Ga_2O_3. The distance between the two nearest tetrahedral sites in the β-phase is 3.612 Å, while that in the γ-phase is 3.564 Å. Because of this 1.3% lattice mismatch, the growth of γ on β would ultimately entail the formation of domain boundaries or shifts of the γ structure. As a TEM image captures the projection of all atoms in the column along a thickness of ~20–100 nm, shifts of lattice planes at different thicknesses would also result in a unique signature structure in projection. Such an overlap results in Fig. 1(d), where three Ga atoms—octahedral Ga sitting in between two tetrahedral Ga sites—form a diagonal, ladder-like crystal structure, which we see often in our films.

Similar to the superimposed structure in Fig. 1(d), a combined lattice shift of β-Ga_2O_3 [010] sheets across a stacking fault in the ⟨102⟩ direction[27,28] can create new superimposed structures. These structures, as shown in Figs. 2(b) and 2(c), superficially resemble those of γ-Ga_2O_3 in Fig. 2(a) as they all have a bright atomic site in the middle. Thus, when seen in noisy or low-resolution TEM images, one can easily misinterpret the phases. The high-resolution HAADF-STEM images show a clear difference between the three crystal structures. The 2D-projected repeat unit for each crystal structure is outlined by yellow dotted lines on the HAADF-STEM images and black solid lines in the crystal model. γ-Ga_2O_3 is characterized by an edge-sharing hexagonal beehive structure where the four side-edges have three Ga atoms lined up in a straight line. The outline of the superimposed structure in Fig. 2(b) may seem to have a similar hexagonal repeat unit with the octahedral site in the middle, but they have rounded side-edges, and the actual projected repeat unit is a parallelogram. The structure in Fig. 2(c) has four atoms in the side-edges and has a distorted hexagonal repeat unit in projection. The different locations of the oxygen atoms also reinforce these differences. Based on understanding the differences of the crystal structures, we determined γ-phase inclusions in our series of samples discussed in this paper.

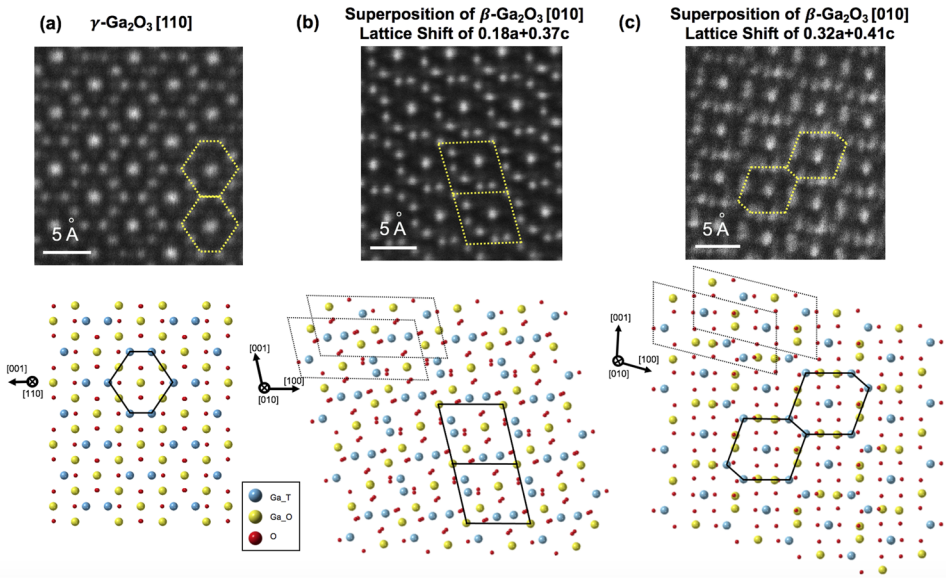

FIG. 2. Comparison of the γ-Ga_2O_3 crystal structure to two differently superimposed β-Ga_2O_3 lattice structures separated by a stacking fault by aberration-corrected STEM images and crystal models. The 2D-projected repeat unit for each crystal structure is outlined by yellow dotted lines on the HAADF-STEM images and black solid lines in the crystal model. (a) γ-Ga_2O_3 is characterized by an edge-sharing hexagonal honeycomb structure where the four side-edges have three Ga atoms arranged in a straight line. (b) Superimposed lattice structure after net lattice shifts of 0.18a and 0.37c along the a and c directions, respectively. The black dotted lines outline the unit cell of β-Ga_2O_3. Although the outline of the crystal structure is superficially similar to hexagonal γ-Ga_2O_3, this crystal structure has rounded side-edges and the 2D-projected repeat unit is not hexagonal. (c) Superimposed lattice structure after combined lattice shifts of 0.32a and 0.41c (or 0.18a and 0.58c) along the a and c directions, respectively. This crystal structure has four atoms in the side-edges and has a distorted hexagonal repeat unit in projection.

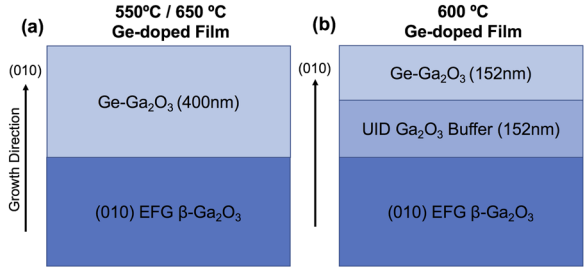

FIG. 3. Crystal growth schematics for Ge-doped β-Ga_2O_3 samples grown at different temperatures. (a) Ge-doped β-Ga_2O_3 films were grown at 550 °C (DG1) and 650 °C (DG3) on Fe-doped β-Ga_2O_3 substrates. The film thickness is 400 nm. (b) Film grown at 600 °C (DG2) has a buffer layer with a thickness same as that of the film to prevent the diffusion of Fe dopants from the substrate.

Doped β-Ga_2O_3

Three Ge-doped β-Ga_2O_3 thin films were grown at different temperatures of 550 °C (DG1), 600 °C (DG2), and 650 °C (DG3), respectively, to understand the temperature effects on the growth and film quality (see Table I for details and film labels). The carrier concentration was on the order of 5×10^{18} cm^{-3} and $\sim 10^{17}$ cm^{-3} for DG1 and DG3 grown films, respectively. DG2 was aimed for $\sim 10^{18}$ cm^{-3} density; however, it was non-conductive, and therefore, the carrier concentration could not be extracted. Figure 3 shows the growth schematics for doped samples. The substrates were Fe-doped EFG β-Ga_2O_3, and as the thickness of DG2 is smaller than the other two, it was grown on a buffer layer to prevent the diffusion of Fe-dopants during growth at high temperatures.[45,46]

Figures 4(a)–4(f) show the HAADF-STEM images of the Ge-doped β-Ga_2O_3 films (DG1–DG3) grown at 550 °C, 600 °C, and 650 °C, respectively. Here, we note that a well-developed γ-surface layer was observed across almost all of the TEM lamellae (~10 μm laterally), except for a few regions (100–300 nm laterally) with less pronounced γ-, amorphous, or no surface layers. Such a region in DG2 is shown in Fig. S2 of the supplementary material. High magnification HAADF-STEM images in Figs. 4(a), 4(c), and 4(e) show all three films having γ-phase structures on the surface of the films. The thickness of the γ-phase surface layer is 5, 7, and 1 nm on average for Ge-doped β-Ga_2O_3 films grown at 550 °C, 600 °C, and 650 °C, respectively. The shallow depth of the γ-phase layer in 650 °C grown film (DG3) might be explained as a higher growth temperature suppressing the formation of the γ-phase while thermodynamically stabilizing the β-phase. This could also be a direct effect of the film having a lower Ge-doping concentration of $\sim 10^{17}$ cm^{-3}; however, we note that the same layer thickness was seen in the film with $\sim 10^{20}$ cm^{-3} Si dopant concentration compared to the unintentionally doped (UID) β-Ga_2O_3 with an unmeasurably low Si

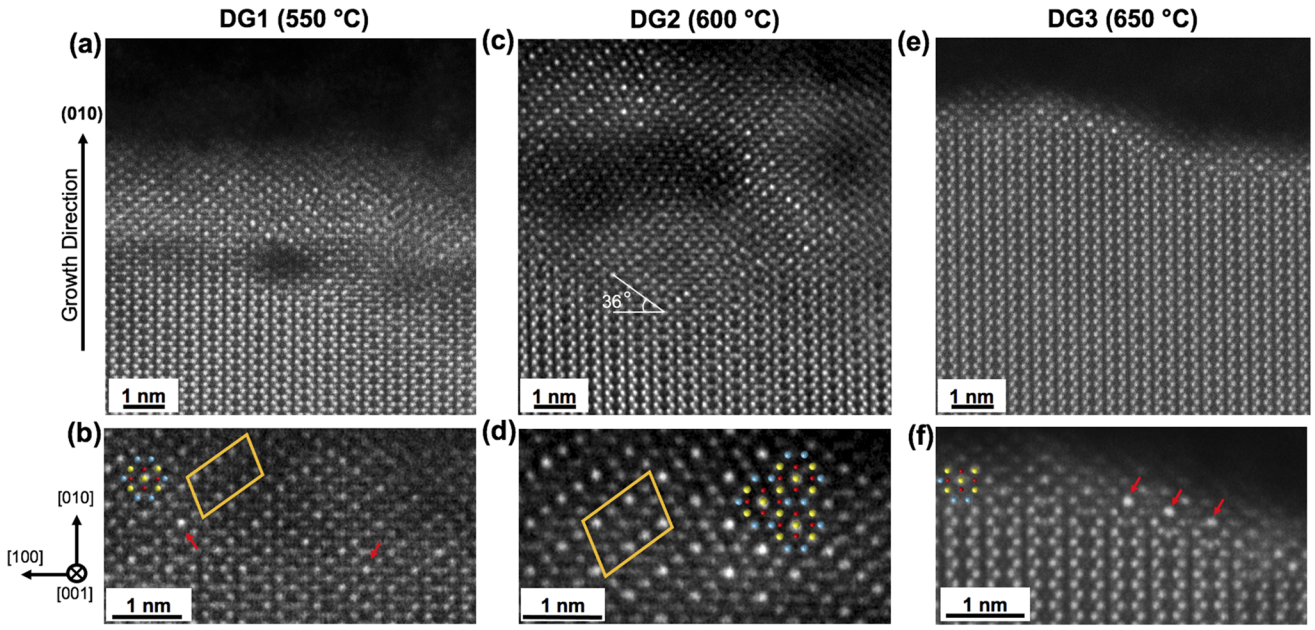

FIG. 4. Comparison of Ge-doped β-Ga_2O_3 samples grown at different temperatures. All three samples show γ-phase formations at the film surface. [(a) and (b), (c) and (d), and (e) and (f)] Films grown at 550 °C (DG1), 600 °C (DG2), and 650 °C (DG3), respectively. Enlarged surfaces are shown in (b), (d), and (f). A distinguishable γ-Ga_2O_3 lattice structure can be observed on top of β-Ga_2O_3 in DG1 and DG2, as in (a) and (c), which is further enlarged to (b) and (d) to show the crystal structures including the misaligned γ lattice structure discussed in Fig. 1(d). In (c), the angle between the (010) surface of β-Ga_2O_3 and the onset formation plane of γ-Ga_2O_3 is estimated to be ~36°, which corresponds to β-(310) and γ-($1\bar{1}0$) planes. See Fig. 8 for more details. The red arrows in (b) and (f) point to the bright octahedral Ga sites in the γ-phase. γ-phase formation in (b) was observed near the surface and inside the film (Fig. S3), while in (f), an onset of γ-phase (~1 nm) was observed only on the surface. The γ-phase structure is partially overlaid in Fig. 4(f). The extra atom on top of the structure is likely from a region of the γ-phase that is offset vertically by half a unit cell and overlapping in projection. All three samples show Ga interstitials near the γ-phase, which can be found in (a), (c), and (e).

dopant concentration and an unintentional B dopant concentration of ~10^{16} cm^{-3}.[34]

To determine the role of dopants in the formation of the γ-phase, we extended our study to grow films with other dopants. Two samples, Sn-doped β-$(Al_{0.15}Ga_{0.85})_2O_3$ (DSn) and Si-doped β-Ga_2O_3 (DSi), were grown on buffer layers and EFG (010) β-Ga_2O_3 substrates at growth temperatures of 550 °C and 650 °C, respectively. The carrier concentration for DSn and DSi was 2×10^{18} cm^{-3} and 2×10^{20} cm^{-3}, respectively. We also examined an unintentionally doped (UID) β-Ga_2O_3 film grown at 575 °C with a B dopant concentration of ~10^{16} cm^{-3} and all other impurity levels below the detection limits of secondary ion mass spectroscopy (SIMS).[34] In the low magnification TEM image [Fig. 5(b)], we can see the formation of a distinct surface layer on Sn-doped β-$(Al_{0.15}Ga_{0.85})_2O_3$ (DSn) similar to the Ge-doped samples grown at 550 °C (DG1) and 600 °C (DG2). On the surface of Si-doped β-Ga_2O_3 (DSi) in Fig. 5(h), we can see an onset of γ-phase formation by the appearance of the octahedral Ga site in the middle of the hexagon. The UID β-Ga_2O_3 shows a thin γ-phase at the surface,[34] which is also similar to Ge-doped β-Ga_2O_3 grown at 650 °C (DG3). The γ-phase in all three samples (DSn, DSi, UID β-Ga_2O_3) covered most of the observed region (~10 μm laterally) except for a few regions (Fig. S2).

As shown in Fig. 4(c), films with a thick layer of γ-phase show that the γ-phase tends to nucleate along 36° from the (010) plane of β-Ga_2O_3. This angle of plane corresponds to the $(1\bar{1}0)$ plane of the γ-phase and the (310) plane of β-Ga_2O_3. This will be made clear in Fig. 8, where we show a similar but enlarged area. We also add that at the interfaces of γ and β-Ga_2O_3 in all of the doped samples, we observe high densities of interstitials in β-Ga_2O_3, which we believe is correlated with the γ-phase formation. We will discuss this in more detail in the section titled Correlation of Ga interstitials to the formation of γ-Ga_2O_3.

It is important to note here that our series of undoped β-$(Al_xGa_{1-x})_2O_3$ films discussed later in this study did not show any

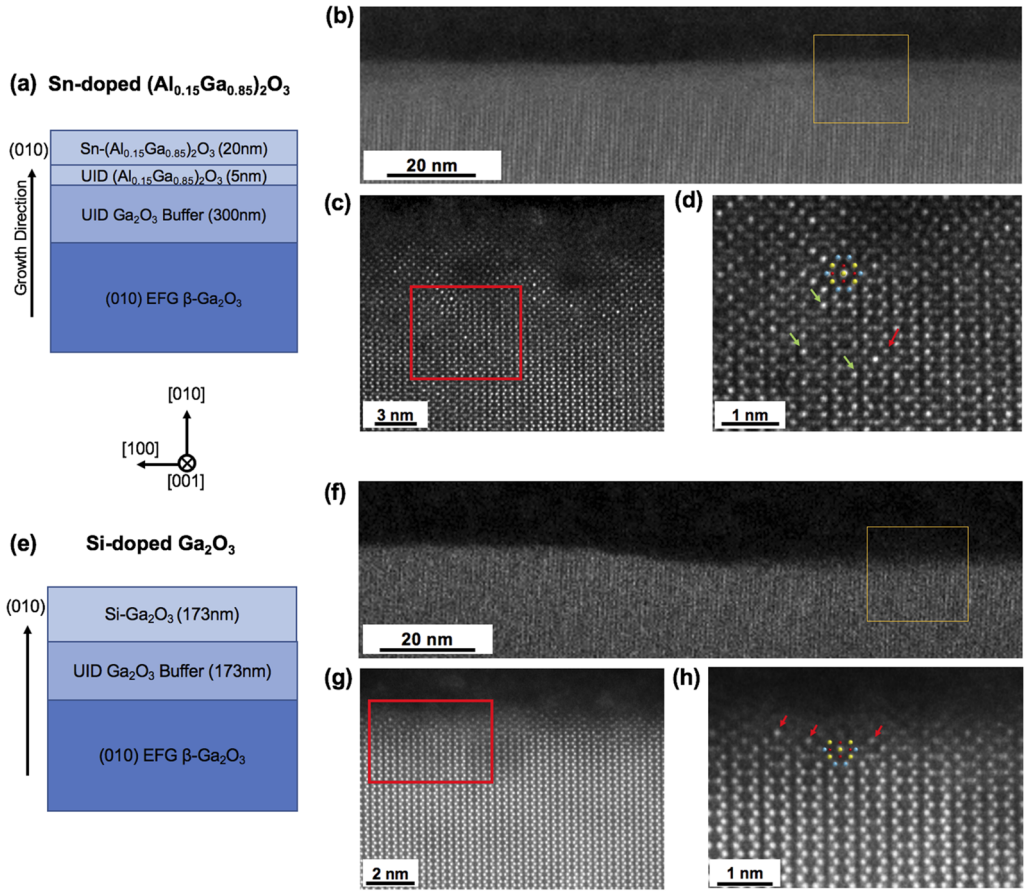

FIG. 5. Sn-doped β-$(Al_{0.15}Ga_{0.85})_2O_3$ (DSn) sample and Si-doped β-Ga_2O_3 (DSi) sample showing γ-phase formations at the film surface. (a) Growth schematic of DSn grown at 550 °C. This sample also shows (b) a distinct surface layer of γ-$(Al_xGa_{1-x})_2O_3$, which is enlarged in (c). (d) Inclusion of the gamma phase on the surface as well as inside the β-phase crystalline structure shown by a red arrow. The green arrows point to octahedral Ga atomic sites that have higher contrast compared to other Ga sites, suggesting they are Sn-dopants occupying the octahedral sites. DSi was grown at 650 °C with a buffer layer as in (e). (f) The low magnification image does not show a distinct γ-Ga_2O_3 layer on the surface. [(g) and (h)] Onset of the γ-phase by nucleation at bright octahedral Ga sites. This observation is similar to Ge-doped β-Ga_2O_3 grown at 650 °C (DG3) [Fig. 4(f)].

surface layers of γ-Ga_2O_3. However, Sn-doped β-$(Al_{0.15}Ga_{0.85})_2O_3$ does show γ-Ga_2O_3 on the surface. This suggests that Sn-dopants may contribute to promoting surface γ-Ga_2O_3 growth. In fact, while the previous three Ge-doped samples showed the formation of the γ-phase only on the surface of the sample, Sn-doped β-$(Al_{0.15}Ga_{0.85})_2O_3$, which has a low-temperature growth, also shows γ-like defects appearing inside the columns of β-$(Al_{0.15}Ga_{0.85})_2O_3$. In Fig. 5(d), this region is pointed out by a red arrow. A crystal structure from Fig. 1(c) is overlaid as guide to the eye.

We also note that in Fig. 5(d) there are octahedral Ga sites with brighter contrast than neighboring Ga sites, which are noted by green arrows. These bright octahedral Ga sites can be found close to the surface (an image with a wider field of view is provided as Fig. S3 in the supplementary material). Sn is known to prefer octahedral sites,[47] and as Sn incorporation in bulk Ga_2O_3 is known to be sensitive to doping concentration and growth conditions, previous studies have reported segregation of Sn at the surface.[33,48,49] As mentioned previously, in HAADF-STEM, we get a strong contrast for heavy Sn atoms compared to lighter Ga atoms.[36] A higher density of Sn dopants near the surface could therefore contribute to some of the large difference in contrast seen in bright octahedral Ga sites. More discussion on locating the Sn atoms can be found in the supplementary material (Figs. S4 and S5). As such, surfactant effects of Sn and also Ge dopants[33,48,49] may explain our observation of γ-Ga_2O_3 on the surface; however, the γ-phase surface layers of thickness less than 1 nm even in Si-doped β-Ga_2O_3 suggest that the temperature may play a crucial role in γ-phase formations, regardless of the types of dopants. More systematic study would be needed to confirm our suggestion.

Bhuiyan *et al.* previously reported that the existence of the 90° rotated β-[010] structure from β-[001] caused by a high Al concentration in the β-$(Al_xGa_{1-x})_2O_3$ film could serve as an intermediate state inducing the γ-[110] structure.[26] However, all three of our doped samples show that the transition occurs rather directly, regardless of the β-[010] structure. One possible explanation as to why we see a direct phase transition, particularly on the surface of doped samples, has been suggested by the similarity of the oxygen sublattices of γ-Ga_2O_3 (110) when grown on the β-(010) surface.[50] However, as we will see in the section titled β-$(Al_xGa_{1-x})_2O_3$, γ-$(Al_xGa_{1-x})_2O_3$ does not form on the (010) surface of undoped β-$(Al_xGa_{1-x})_2O_3$. As we discuss in the section titled Correlation of Ga interstitials to the formation of γ-Ga_2O_3, we suspect the γ-phase on the surface may be formed by the out-diffusion/precipitation of Ga interstitials.

As the samples are prepared by FIB, which uses Ga ions to prepare a TEM lamella, questions may arise whether γ-Ga_2O_3 on the surface of doped β-Ga_2O_3 is intrinsic to growth or a result of ion beam damage. Since we have used the same sample preparation method for doped and alloyed samples, the presence of the γ-phase only in doped film surfaces suggests that such a possibility is unlikely. In addition, the comparison of doped β-Ga_2O_3 films to that of undoped would be necessary to complete the understanding of dopants and the formation mechanism of the γ-phase; however, the growth in the current MBE systems in the presence of ion sources would result in unintentionally doped (UID) β-Ga_2O_3 films. The lowest UID Si-doped film achievable in our system had a doping density below the detection limit of SIMS ($<\sim10^{15}$ cm^{-3}), which still showed the formation of the γ-phase surface layer.[34]

β-$(Al_xGa_{1-x})_2O_3$

We now discuss β-$(Al_xGa_{1-x})_2O_3$ ($x < 20\%$) epitaxial films grown on β-Ga_2O_3 substrates to compare the formation mechanism of γ-phase to that of the doped samples. Three β-$(Al_xGa_{1-x})_2O_3$ films were grown for an hour at 500 °C (A1), 600 °C (A2), and 700 °C (A3), respectively. Crystal growth schematics are shown in Fig. 6(a). Sample A1 was grown on the Sn-doped (010) β-Ga_2O_3 substrate, while A2 and A3 were grown on Fe-doped (010) β-Ga_2O_3 substrates. The thicknesses of the β-Ga_2O_3 buffer layers are approximately half the thicknesses of the β-$(Al_xGa_{1-x})_2O_3$ films, as the growth rate of both β-$(Al_xGa_{1-x})_2O_3$ and UID Ga_2O_3 is similar. The films showed several orders of Pendellösung fringes indicating high quality, uniform films with smooth interfaces, as shown in Fig. 6(b). The thicknesses of the films were determined by fitting the measured XRD 2θ-ω scans using the xrayutilities Python package[51] to be ~32 nm, 55 nm, and 37 nm, respectively. The corresponding

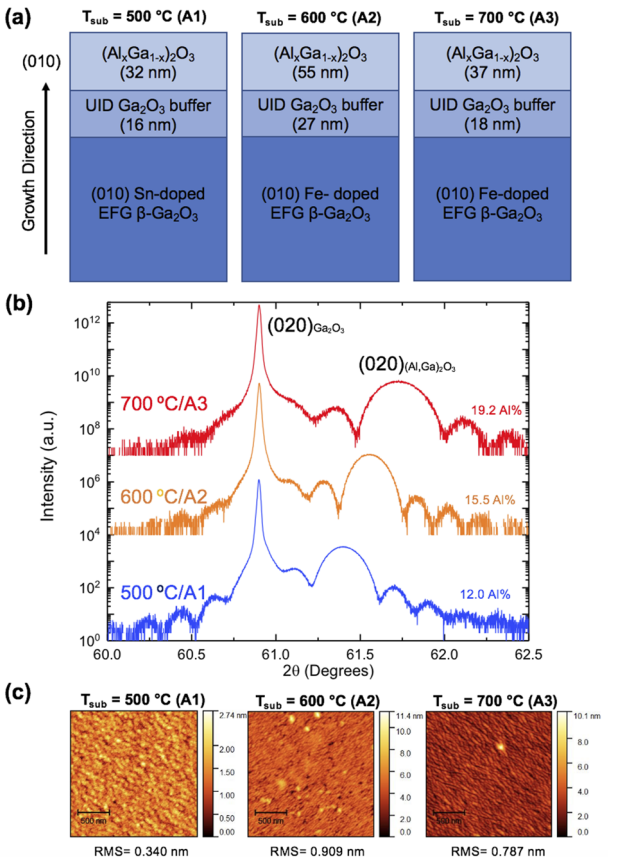

FIG. 6. (a) Crystal growth schematics for series A1–A3. A1 was grown on the Sn-doped (010) β-Ga_2O_3 substrate, while A2 and A3 were grown on the Fe-doped (010) β-Ga_2O_3 substrate. (b) 2θ-ω XRD scans show the shift in the β-$(Al_xGa_{1-x})_2O_3$ (020) peak as T_{sub} is changed from 500 to 700 °C as well as a change in thickness for the film grown at 700 °C. (c) Comparison of 2 × 2 μm^2 AFM scans. Films are smooth at all growth temperatures, but typical surface morphologies showing elongated islands become more prominent at T_{sub} = 600 °C and higher.

Al concentrations (A1–A3) of 12.0%, 15.5%, and 19.4% were extracted using the separation of the (020) β-$(Al_xGa_{1-x})_2O_3$ and the (020) Ga_2O_3 Bragg angle peaks from a symmetric 2θ-ω scan, as described by Oshima *et al.*[52] The decrease in growth rate (as shown in Table I) and the increase in Al content with the increase in substrate temperature is attributed to the increase in the desorption of the volatile Ga_2O suboxide with increasing substrate temperature, which leads to a lower Ga concentration on the growth surface and an increased Al:Ga ratio.[30] AFM measurements in Fig. 6(c) showed a similar surface morphology for all three films with sub-nanometer roughness over a $2 \times 2\ \mu m^2$ scan area. The rms values for the films were 0.340, 0.909, and 0.787 nm for the films A1–A3, respectively. All films showed an elongated island growth in-plane, which is typically seen in Ga_2O_3 and $(Al_xGa_{1-x})_2O_3$ grown on (010) oriented surfaces by MBE.[32,33]

The β-$(Al_xGa_{1-x})_2O_3$ samples were imaged by HAADF-STEM for atomic scale observations. The bulk of the film is in the β-phase aligned with the substrate. Consistent with an island growth/nucleation, sample A1 grown at 500 °C shows V-shaped regions between the ordered phase, and these contain polycrystalline inclusions, as shown in Figs. 7(a) and 7(b). Although the TEM sample was cut along the (001) surface, such that the majority of the film is viewed along β-[001], inside the V-shaped regions, we also see the coexistence of β-[010] and γ-[110] as in Fig. 7(c). An extremely high density of Ga interstitials was observed (Fig. S6) in the β-phase near the transition to γ-[110].

TEM images of sample A2 grown at 600 °C display a reduced fraction of V-shaped defect regions, and these still include some γ-phase at a frequency of approximately one region per 300 nm with a standard deviation of the mean of 48 nm in the lateral direction, as shown in Fig. 7(d). The regions showing the γ-Ga_2O_3 crystal structure are highlighted by red arrows in Fig. 7(f). We also note that while there were few Ga interstitials overall, they are still notably present near the γ-phase interface.

Sample A3 grown at 700 °C is the most uniformly grown of the three samples without any secondary phase inclusions. However, we observed the high density of uniformly distributed Ga interstitials throughout the film, as pointed out by yellow arrows in Fig. 7(i).

As we were able to get an inclusion-free, uniformly grown film at 700 °C, we expect that higher growth temperatures should eliminate the formation of the γ-phase, as γ-Ga_2O_3 can be annealed out

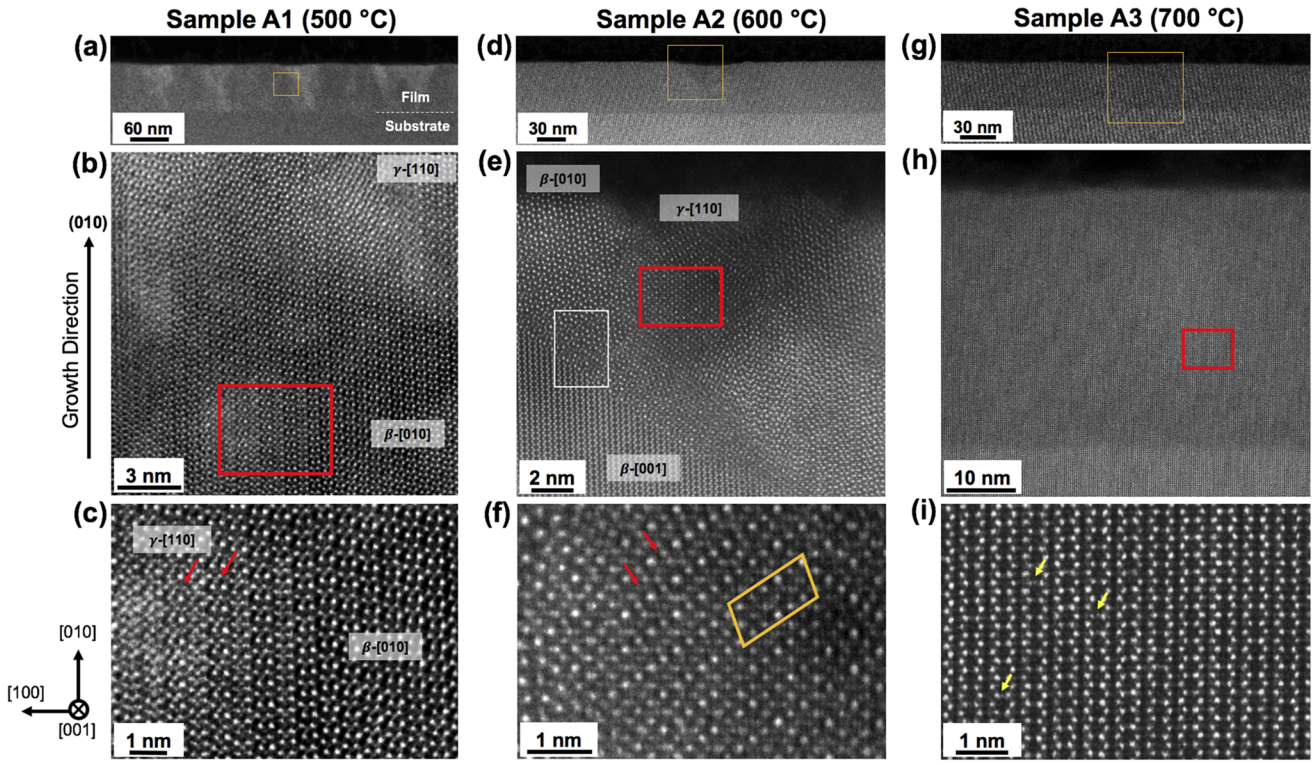

FIG. 7. Samples A1–A3 (500–700 °C) grown with increasing temperature reveal different characteristics in TEM images. [(a) and (c), (d) and (f), and (g) and (i)] A1, A2, and A3, respectively. The boxed region in (a), (d), and (g) enlarges to (b), (e), and (h) then to (c), (f), and (i). Overview of sample A1 (500 °C) in (a) shows large regions of polycrystalline inclusions. The enlarged image in (b) and (c) shows the mixture of β [010] and γ [110]-crystal zones, where the actual crystal zone for this projection should be β [001]. Sample A2 (600 °C) in (d) shows a cleaner film than in (a); however, it has V-shaped defect regions. (e) Inside of the V-region where the formation of both β [010] and γ [110] phases has occurred. The region inside the white box will be discussed later in Fig. 8. (f) The enlarged area inside the V-region shows the crystal structure of γ-Ga_2O_3 [110] and superimposed γ-Ga_2O_3 [110]. Sample A3 (700 °C) in (g) and (h) shows a uniformly grown film. (i) Although the film does not suffer from γ-phases, it shows a high density of Ga interstitials. The red arrows in (c) and (f) point to the γ [110] crystal structure, while the yellow arrows in (i) point to Ga interstitials.

at higher temperatures.[44] We also focus on the fact that samples A1 and A2 have low Al concentrations (x < 20%), yet they both showed inclusions of the γ-phase, while Ref. 26 did not observe inclusions of the γ-phase below (x < 27%). This suggests that the γ-$(Al_xGa_{1-x})_2O_3$ formation could be more dependent on the growth conditions rather than the Al composition.

The formation of γ-$(Al_xGa_{1-x})_2O_3$ in the growth of β-$(Al_xGa_{1-x})_2O_3$ is not yet fully understood. Bhuiyan *et al.*[26] suggested that the Al substitution may create a strain to rotate β-Ga_2O_3 [001] into [010] and that the strain can then further trigger the transformation of β-Ga_2O_3 [010] into γ-Ga_2O_3 [110]. We also observe regions of β-$(Al_xGa_{1-x})_2O_3$ [010] phases nearby γ-$(Al_xGa_{1-x})_2O_3$ [110], but given the authors' challenges in Ref. 26 distinguishing the overlap of multiple faulted β-$(Al_xGa_{1-x})_2O_3$ [010] structures from that of γ-$(Al_xGa_{1-x})_2O_3$ [110], a careful analysis still needs to be done to understand the extent of strain effects caused by Al substitution.

While sample A1 shows only a small fraction of γ-Ga_2O_3 inclusions uniformly distributed within the film, sample A2 shows the localized growth of γ-Ga_2O_3 inside the V-shaped regions. The edges of the V-shapes form either 54° or 33°–37° with the (010) surface, which are quite close to that of $(41\bar{2})$ and (310) planes in β-$(Al_xGa_{1-x})_2O_3$. These planes resemble the planes forming etch pits in bulk β-Ga_2O_3, as previously reported by Hanada *et al.*,[53] suggesting that these planes have preferably lower surface energies. Along these planes, β-$(Al_xGa_{1-x})_2O_3$ [001] is either seen to rotate to β-[010] or transform into γ-$(Al_xGa_{1-x})_2O_3$ [110]. In particular, along the β-(310) planes, we see the formation of γ-$(Al_xGa_{1-x})_2O_3$, as shown in Fig. 7(e) and also in Fig. 8, showing an enlarged area inside the white boxed region in Fig. 7(e). The $(1\bar{1}0)$ plane of the γ-phase is observed to start on the (310) plane of β-$(Al_xGa_{1-x})_2O_3$ (red arrows), which then rotates 107° to form a cluster of [110]-projected structures.

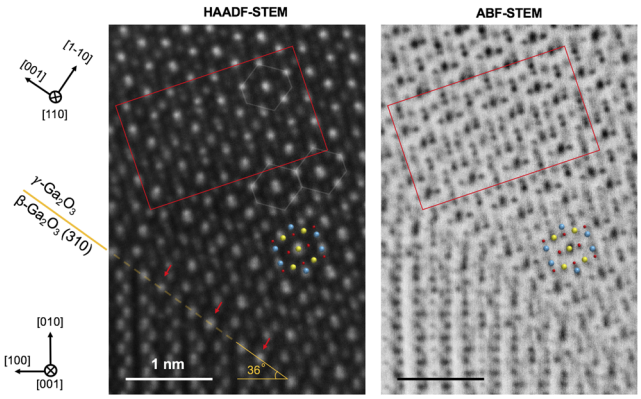

FIG. 8. Observation of angled γ-$(Al_xGa_{1-x})_2O_3$ formation directly on sample A2 (600 °C), β-$(Al_{0.16}Ga_{0.84})_2O_3$. This shows an area enlarged from the white box in Fig. 7(e). The bottom right corner is slightly out of focus in the ABF-STEM image due to sample tilt. The lower left side shows the crystal structure of β-Ga_2O_3 [001]. γ-$(Al_xGa_{1-x})_2O_3$ is observed to grow directly on the angled surface of sample A2, as shown by red arrows and orange dotted line. Because the nucleation of γ-phase happens out-of-phase at different sites, several layers of γ-$(Al_xGa_{1-x})_2O_3$ [110] with different lattice shifts become superimposed, as can be seen inside the red boxed area. This results in different intensities of Ga atomic sites in γ-$(Al_xGa_{1-x})_2O_3$. The white outline of the γ-phase repeat unit is overlaid in the HAADF-STEM image to aid the comparison of atomic intensities with that shown in Fig. 1(c).

Although the atomic column intensities of a region in sample A2 shown in Fig. 8 are different from what we expect for a single γ-Ga_2O_3 [110]-projected structure, the ABF-STEM image clearly shows that the region is dominated by the γ-phase. The different atomic column intensity is due to several out-of-phase formations of the γ-phase on the surface of β-Ga_2O_3 (310), leading to superposition of γ-Ga_2O_3 [110] sheets with different combinations of lattice shifts. The boxed area in red shows the lattice shifts happening in the ABF-STEM image. As a result, HAADF-STEM images taken in projection suffer from different atomic column intensities from that of the original single-grain lattice structure. Here again, we note that determining the crystal structure by depending on the atomic column intensity in HAADF-STEM images is not recommended as the image intensity can be affected largely by the superimposed crystal structure as well as the concentration of Al and the actual position of Al along the column that can affect the channeling of the electron probe. Rather, by ABF-STEM imaging, we can identify the phases by obtaining the full crystal structure, with all lattice sites including the oxygen, visible.

Correlation of Ga interstitials to the formation of γ-Ga_2O_3

Both in doped and alloyed films, we have frequently observed Ga interstitials in the β-phase structure near the region where transitions from β to γ would occur. Thus, for doped films, the interstitials were observed near the surface, while for alloyed samples A1 and A2, the interstitials were found inside the film near the phase-transition boundary. Sample A1 had excessive Ga interstitials as shown in Fig. S6. Although sample A2 had a few Ga interstitials, they were only found near the V-shaped regions. Sample A3 also had a high density of Ga interstitials, but as there were no γ-phase, it was rather uniformly distributed in the film.

Figure 9(a) presents the interstitial position in the crystal schematic of β-Ga_2O_3 in the crystal zones [010] and [001]. Here, the blue Ga sites are tetrahedral Ga sites, while the yellow Ga sites are octahedral Ga sites. Both cross section [001] and plan-view [010] TEM samples were prepared from Sn-doped β-$(Al_{0.15}Ga_{0.85})_2O_3$ (DSn). As shown in Fig. 9(b), a high density of Ga interstitials along a column is observed in plan-view [010]. As shown in cross section [001], Fig. 9(c) shows highly occupied interstitial sites with the intensity of interstitials comparable to that of the Ga atoms nearby. However, the reason for having such a high density of Ga interstitials along a single column and also the high density of occupied interstitial sites, i.e., why the interstitials cluster, is not yet clearly understood.

It is worth noting that β-Ga_2O_3 can support point-defect complexes including a divacancy-interstitial complex where one cation interstitial atom is paired with two cation vacancies, especially in the presence of Sn dopants.[54] Of the complexes studied, the $2V_{Ga}^{T}$–Ga_i defect complex having a vacancy with a neighboring Ga displaced from its tetrahedral site (to create a second Ga vacancy) and moved to an octahedral interstitial site has the lowest formation energy. In HAADF-STEM, we can easily identify interstitial atoms, while it is difficult to image the vacancies on an otherwise occupied column.

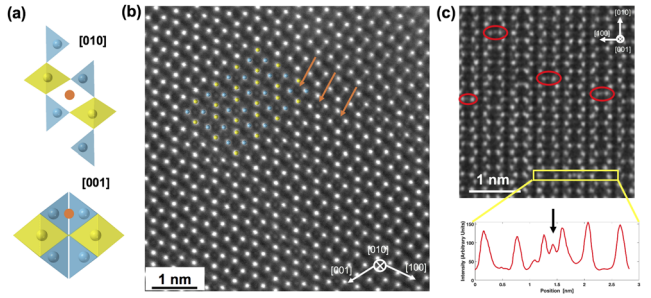

FIG. 9. High densities of Ga interstitials observed in the Sn-doped β-$(Al_{0.15}Ga_{0.85})_2O_3$ (DSn) sample. (a) Crystal structure of β-Ga_2O_3 in the [010] and [001] crystal zones showing interstitial positions, as shown by the orange atom. The blue atoms correspond to tetrahedral Ga, while the yellow atoms are octahedral Ga.[56] (b) High densities of interstitials are observed in plan-view [010] DSn. The arrows are overlaid as guide to the eye. (c) In cross section [001] of DSn, we can see the Ga interstitials in red-circled areas. The line profile of an atomic row at the bottom shows considerable contrast from interstitial site compared to that of the two Ga columns nearby, i.e., there are multiple interstitials viewed in projection along the column.

Therefore, it is likely that the interstitials we observe are a part of this split-vacancy $2V_{Ga}^{T}$–Ga_i defect complex, given their similar structure to those imaged in Ref. 54. Sn-, Ge-, and Si-dopants can either stimulate the formation of the $2V_{Ga}^{T}$–Ga_i defect complexes[54] or form an additional $2V_{Ga}^{T}$–D_i (D: Sn-,[54,55] Si-dopants[55]) complex. Either way, dopants may provide another possible mechanism for increasing the population of the observed interstitials.

To investigate the behavior of Ga interstitials and its relationship to γ-phase formation, we have performed *ex situ* heating of TEM samples prepared from Sn-doped β-$(Al_{0.15}Ga_{0.85})_2O_3$. The samples used for the *ex situ* heating study were TEM lamellae having dimensions of 10 μm (length) × 5 μm (height) and 100 nm in average for the width. Such a small volume would pose restrictions on the migration of interstitials compared to the bulk. This enables us to detect the changes or movements of the interstitials more easily. In addition, the interstitials in our experiment would experience more migration toward the surface than in bulk, leading to a much larger formation of the γ-phase if interstitials do play a role.

After acquiring HAADF-STEM images at room temperature, we heated the samples in an Ar atmosphere up to 200 °C and imaged it again. After seeing no changes, we once again heated up to 400 °C in Ar and then imaged it again after cooling. For accurate comparison, the same region was observed in each case. Figure 10 shows the resulting HAADF-STEM images. At room temperature, we observed the surface was terminated with the uppermost unit cell in the γ-phase, as shown in Fig. 10(a). After being heated up to 200 °C as in Fig. 10(b), the surface in the same region is essentially unchanged. However, after the 400 °C anneal, as shown in Fig. 10(c), a 5–8 nm-thick layer of the γ-phase had formed, which was grown above the original surface. More images are shown in Fig. S7.

The likely origin of this extra γ-phase layer is the interstitials observed in the bulk of the β-phase that have been migrated toward the surface. The more open γ-phase is likely to allow faster diffusion and growth kinetics at intermediate temperatures. Figure 4 suggests that by 650 °C, the β-phase dominates again. To obtain an

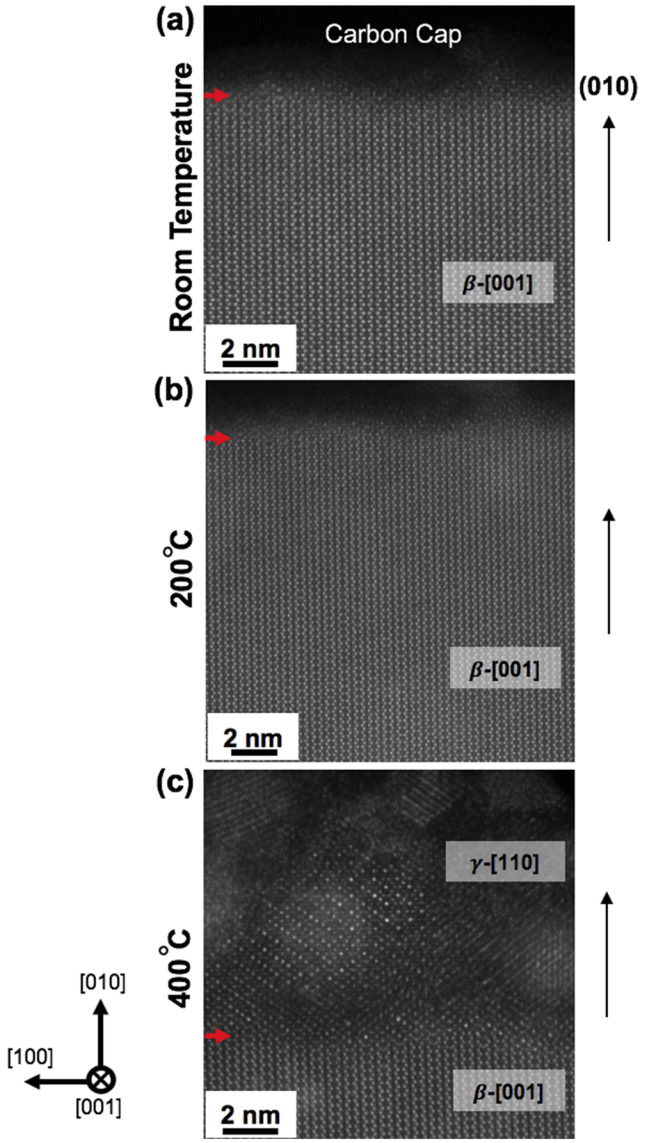

FIG. 10. *Ex situ* heating results of the same region of a Sn-doped β-$(Al_{0.15}Ga_{0.85})_2O_3$ (DSn) TEM cross section. Both (a) the surface at room temperature and (b) the surface after being heated up to 200 °C show only a γ-like surface termination. (c) After heating up to 400 °C, we see the formation of a thick (~5–8 nm) γ-phase region above the original surface. The red arrows indicate the approximate location of the original surface—i.e., the γ-phase has grown on top of the β-phase, presumably from the out-diffusion of interstitials, some of which are still present near the interface. Note the similar small island of the γ-phase on the right in each image.

estimate of changes in the interstitial density, we turn to some subtle details of our STEM imaging. In STEM, we use a finely focused probe to scan across the sample in a raster pattern to obtain images. However, imaging interstitials under an electron microscope with a beam energy of 300 keV can be challenging as the energy of the electron beam is sufficient to displace the interstitials, causing them

to occasionally hop around from one interstitial site to another. We maintained the same voltage, current, and dwell time each time we imaged the samples so that the energy delivered to an interstitial site remained the same. We were not able to see much evidence of hopping of the interstitials in the sample before and after being heated up to 200 °C. However, frequent hopping was observed in the sample after being heated up to 400 °C.

In Fig. 9(b), we have seen that at room temperature there is a high density of interstitials along a column as well as a high density of occupied interstitial sites in the film, as shown in Fig. 9(c). As TEM sees atoms in projection, if the interstitials are hopping to a nearby interstitial site, where other interstitial sites in the same column are already occupied, the contrast change would be low and we would not be able to observe the hopping clearly. Even if one or two interstitials left the original position, we would still detect the remaining interstitials at the previous site, so the change in contrast would be small. Imaging the sample after heating up to 400 °C still showed a similar fraction of occupied columns; however, the intensity fluctuations from hopping were much easily observed. This implies that after the 400 °C anneal, we have a reduced density of interstitials along any given column.

As the growth of the γ-phase occurred when the number of interstitials decreased (i.e., 400 °C) and it grew above the original surface, rather than as a conversion of the existing β-phase, we suspect that the γ-phase was constructed from the out-diffusion and coalescence of interstitials. The growth of γ-phase at ~400 °C suggests that some care must be taken to control local heating to avoid the possibility of device degradation while in operation. Although the typical operating temperature of a device is around 100–200 °C, the low thermal conductivity of β-Ga_2O_3 in combination with high voltage, high current conditions for extended periods could raise the temperature to a point where the γ-phase growth from interstitial diffusion and coalescence could occur at interfaces such as metal contacts. Therefore, all effort should be made to avoid the formation of the γ-phase.

CONCLUSIONS

In summary, we have observed γ-phase inclusions in MBE-grown Ge- and Si-doped β-Ga_2O_3 films, Sn-doped β-$(Al_{0.15}Ga_{0.85})_2O_3$, and a series of β-$(Al_xGa_{1-x})_2O_3$ films grown at different temperatures. The inclusion of the γ-phase in most samples shows that it is a widely occurring structural defect during the growth of β-Ga_2O_3. The formation of a surface γ-phase is found in doped samples, especially at growth temperatures below 650 °C. We also observed γ-$(Al_xGa_{1-x})_2O_3$ formation between nucleating islands of β-$(Al_xGa_{1-x})_2O_3$ grown at temperatures below 650 °C. From the trend observed in all our doped β-Ga_2O_3 and β-$(Al_xGa_{1-x})_2O_3$ films, increasing the substrate temperature leads to a reduction in γ-phase inclusions and improved the film crystalline quality and uniformity. The appearance of the γ-phase at lower temperatures suggests that the γ-phase would be the early forming phase in terms of kinetics. This idea is further strengthened by our observation of the γ-phase growth above the original surface of Sn-doped β-$(Al_{0.15}Ga_{0.85})_2O_3$ when heated up to a relatively low temperature of 400 °C, likely formed from the out-diffusion/precipitation of interstitials, again suggesting that the more-open γ-phase was kinetically favored over the more thermodynamically stable β-phase. Further studies are required to understand and control the energetics and the kinetics of the γ-phase through modeling and simulation.

AUTHORS' CONTRIBUTIONS

C.S.C. and N.T. contributed equally to this work.

SUPPLEMENTARY MATERIAL

See the supplementary material for more information on HAADF-STEM images of doped and alloyed samples.

ACKNOWLEDGMENTS

This work was primarily supported by the Cornell/AFOSR ACCESS center of excellence (Grant No. FA955018-1-0529). This work made use of the Cornell Center for Materials Research (CCMR) Shared Facilities, which are supported through the NSF MRSEC Program (Grant No. DMR-1719875). The FEI Titan Themis 300 microscope was acquired through Grant No. NSF-MRI-1429155, with additional support from Cornell University, the Weill Institute, and the Kavli Institute at Cornell. S.M. and T.J.A. are thankful for the support of OSD seeding grant entitled "150 Volt Ultra-wide Bandgap High-Efficiency RF Amplifier Technology." We also thank Y. Yao from Cornell University for the help with *ex situ* heating using their heating furnace.

DATA AVAILABILITY

The data that support the findings of this study are available within the article and its supplementary material and from the corresponding author upon reasonable request.

REFERENCES

[1] S. Yoshioka, H. Hayashi, A. Kuwabara, F. Oba, K. Matsunaga, and I. Tanaka, J. Phys.: Condens. Matter **19**, 346211 (2007).
[2] R. Roy, V. G. Hill, and E. F. Osborn, J. Am. Chem. Soc. **74**(3), 719–722 (1952).
[3] M. Zinkevich and F. Aldinger, J. Am. Ceram. Soc. **87**, 683 (2004).
[4] M. Higashiwaki, K. Sasaki, A. Kuramata, T. Masui, and S. Yamakoshi, Appl. Phys. Lett. **100**, 013504 (2012).
[5] W. S. Hwang, A. Verma, H. Peelaers, V. Protasenko, S. Rouvimov, H. Grace Xing, A. Seabaugh, W. Haensch, C. V. de Walle, Z. Galazka, M. Albrecht, R. Fornari, D. Jena, and D. Jena, Appl. Phys. Lett. **104**, 203111 (2014).
[6] A. J. Green, K. D. Chabak, E. R. Heller, R. C. Fitch, M. Baldini, A. Fiedler, K. Irmscher, G. Wagner, S. E.Tetlak, A.Crespo, K.Leedy, and G. H.Jesse, IEEE Electron Device Lett. **37**, 902 (2016).
[7] W. Li, K. Nomoto, Z. hu, T. Nakamura, D. Jena, and H. G. Xing, in *IEEE International Electron Devices Meeting (IEDM)* (IEEE, 2019), pp. 12.3.1–12.4.4.
[8] W. Li, Z. Hu, K. Nomoto, R. Jinno, Z. Zhang, T. Q. Tu, K. Sasaki, A. Kuramata, D. Jena, and H. G. Xing, in *IEEE International Electron Devices Meeting (IEDM)* (IEEE, 2018), pp. 8.5.1–8.5.4.
[9] J. K. Mun, K. Cho, W. Chang, H.-W. Jung, and J. Do, ECS J. Solid State Sci. Technol. **8**, Q3079 (2019).
[10] Z. Hu, H. Zhou, Q. Feng, J. Zhang, C. Zhang, K. Dang, Y. Cai, Z. Feng, Y. Gao, X. Kang, and Y. Hao, IEEE Electron Device Lett. **39**, 1564 (2018).
[11] Z. Xia, H. Xue, C. Joishi, J. Mcglone, N. K. Kalarickal, S. H. Sohel, M. Brenner, A. Arehart, S. Ringel, S. Lodha, W. Lu, and S. Rajan, IEEE Electron Device Lett. **40**, 1052 (2019).

[12]W. Lueangchaichaweng, N. R. Brooks, S. Fiorilli, E. Gobechiya, K. Lin, L. Li, S. Parres-Esclapez, E. Javon, S. Bals, G. van Tendeloo, J. A. Martens, C. E. A. Kirschhock, P. A. Jacobs, and P. P. Pescarmona, Angew. Chem. **53**, 1585 (2014).
[13]H. Hayashi, R. Huang, H. Ikeno, F. Oba, S. Yoshioka, I. Tanaka, and S. Sonoda, Appl. Phys. Lett. **89**, 181903 (2006).
[14]T. Oshima, T. Nakazono, A. Mukai, and A. Ohtomo, J. Cryst. Growth **359**, 60–63 (2012).
[15]C. Arean, A. Bellan, M. Mentruit, M. Delgado, and G. Palomino, Microporous Mesoporous Mater. **40**, 35 (2000).
[16]M. Mitome, S. Kohiki, T. Nagai, K. Kurashima, K. Kimoto, and Y. Bando, Cryst. Growth Des. **13**, 3577 (2013).
[17]H. Y. Playford, A. C. Hannon, E. R. Barney, and R. I. Walton, Chem. Eur. J. **19**, 2803–2813 (2013).
[18]T. Oshima, Y. Kato, M. Oda, T. hitora, and M. Kasu, Appl. Phys. Express **10**, 051104 (2017).
[19]A. Mujica, C. J. Pickard, and R. J. Needs, Phys. Rev. B **91**, 214104 (2015).
[20]A. Zoroddu, F. Bernardini, P. Ruggerone, and V. Fiorentini, Phys. Rev. B **64**, 045208 (2001).
[21]A. A. Demkov, O. F. Sankey, J. Gryko, and P. F. McMillan, Phys. Rev. B **55**, 6904 (1997).
[22]Y. Yao, S. Okur, L. A. M. Lyle, G. S. Tompa, T. Salagaj, N. Sbrockey, R. F. Davis, and L. M. Porter, Mater. Res. Lett. **6**, 268 (2018).
[23]Y. Zhuo, Z. Chen, W. Tu, X. Ma, Y. Pei, and G. Wang, Appl. Surf. Sci. **420**, 802–807 (2017).
[24]I. Cora, F. Mezzadri, F. Boschi, M. Bosi, M. Čaplovičová, G. Calestani, I. Dódony, B. Pécz, and R. Fornari, CrystEngComm **19**, 1509 (2017).
[25]I. Cora, Z. Fogarassy, R. Fornari, M. Bosi, A. Rečnik, and B. Pécz, Acta Mater. **183**, 216 (2020).
[26]A. F. M. A. U. Bhuiyan, Z. Feng, J. M. Johnson, H.-L. Huang, J. Sarker, M. Zhu, M. R. Karim, B. Mazumder, J. Hwang, and H. Zhao, APL Mater. **8**, 031104 (2020).
[27]C. Wouters, R. Schewski, and M. Albrecht, APL Mater. **8**, 089101 (2020).
[28]D. Gogova, G. Wagner, M. Baldini, M. Schmidbauer, K. Irmscher, R. Schewski, Z. Galazka, M. Albrecht, and R. Fornari, J. Cryst. Growth **401**, 665–669 (2014).
[29]A. F. M. A. U. Bhuiyan, Z. Feng, J. M. Johnson, H.-L. Huang, J. Sarker, M. Zhu, M. R. Karim, B. Mazumder, J. Hwang, and H. Zhao, APL Mater. **8**, 089102 (2020).
[30]P. Vogt and O. Bierwagen, Appl. Phys. Lett. **108**, 072101 (2016).
[31]Y. Zhang, C. Joishi, Z. Xia, M. Brenner, S. Lodha, and S. Rajan, Appl. Phys. Lett. **112**, 233503 (2018).
[32]S. W. Kaun, F. Wu, and J. S. Speck, J. Vac. Sci. Technol. A **33**, 041508 (2015).
[33]K. Sasaki, M. Higashiwaki, A. Kuramata, T. Masui, and S. Yamakoshi, J. Cryst. Growth **392**, 30 (2014).
[34]P. Vogt, F. V. E. Hensling, K. Azizie, C. S. Chang, D. Turner, J. Park, J. P. McCandless, H. Paik, B. J. Bocklund, G. Hoffman, M.Budde, O.Bierwagen, D.Jena, H. G.Xing, S.Mou, D. A.Muller, S.Shang, Z.Liu, and D. G.Schlom, APL Mater. **9**, 031101 (2021).
[35]N. Kazushiro, K. Goto, R. Togashi, H. Murakami, Y. Kumagai, A. Kuramata, S. Yamakoshi, and A. Koukitu, J. Cryst. Growth **405**, 19 (2014).
[36]E. J. Kirkland, R. F. Loane, and J. Silcox, Ultramicroscopy **23**, 77 (1987).
[37]M. C. Cao, Y. Han, Z. Chen, Y. Jiang, K. X. Nguyen, E. Turgut, G. D. Fuchs, and D. A. Muller, Microscopy **67**(1), i150–i161 (2018).
[38]P. Villars, Pauling file in: Inorganic solid phases, Springer Materials (online database), Springer, Hedelberg Springer Materials https://materials.springer.com/isp/crystallographic/docs/sd_0313635.
[39]H. St, C. O'Neill, and W. A. Dollase, Phys. Chem. Miner. **20**, 541–555 (1994).
[40]S. Stephanov, V. Nikolaev, V. Bougrov, and A. Romanov, Rev. Adv. Mater. Sci. **44**(1), 63–86 (2016).
[41]P. Mazzolini, A. Falkenstein, C. Wouters, R. Schewski, T. Markurt, Z. Galazka, M. Martin, M. Albrecht, and O. Bierwagen, APL Mater. **8**, 011107 (2020).
[42]G. Wagner, M. Baldini, D. Gogova, M. Schmidbauer, R. Schewski, M. Albrecht, Z. Galazka, D. Klimm, and R. Fornari, Phys. Status Solidi A **211**, 27–33 (2014).
[43]M.-Y. Tsai, O. Bierwagen, M. E. White, and J. S. Speck, J. Vac. Sci. Technol. A **28**(2), 354–359 (2010).
[44]H. Y. Playford, A. C. Hannon, M. G. Tucker, D. M. Dawson, S. E. Ashbrook, R. J. Kastiban, J. Sloan, and R. I. Walton, J. Phys. Chem. C **118**, 16188 (2014).
[45]A. Mauze, Y. Zhang, T. Mates, F. Wu, and J. S. Speck, Appl. Phys. Lett. **115**, 052102 (2019).
[46]M. H. Wong, K. Sasaki, A. Kuramata, S. Yamakoshi, and M. Higashiwaki, Appl. Phys. Lett. **106**, 032105 (2015).
[47]J. B. Varley, J. R. Weber, A. Janotti, and C. G. van de Walle, Appl. Phys. Lett. **97**, 142106 (2010).
[48]S. Ohira, N. Suzuki, N. Arai, M. Tanaka, T. Sugawara, K. Nakajima, and T. Shishido, Thin Solid Films **516**, 5763–5767 (2008).
[49]R. Sharma, M. E. Law, M. Xian, M. Tadjer, E. A. Anber, D. Foley, A. C. Lang, J. L. Hart, J. Nathaniel, M. L. Taheri, F. Ren, S. J. Pearton, and A. Kuramata, J. Vac. Sci. Technol. B **37**, 051204 (2019).
[50]T. Kamimura, D. Krishnamurthy, A. Kuramata, S. Yamakoshi, and M. Higashiwaki, Jpn. J. Appl. Phys., Part 1 **55**, 1202B5 (2016).
[51]D. Kriegner, E. Wintersberger, and J. Stangl, J. Appl. Crystallogr. **46**, 1162 (2013).
[52]Y. Oshima, E. Ahmadi, S. C. Badescu, F. Wu, and J. S. Speck, Appl. Phys. Express **9**, 061102 (2016).
[53]K. Hanada, T. Moribayashi, K. Koshi, K. Sasaki, A. Kuramata, O. Ueda, and M. Kasu, Jpn. J. Appl. Phys., Part 1 **55**, 1202BG (2016).
[54]J. M. Johnson, Z. Chen, J. B. Varley, C. M. Jackson, E. Farzana, Z. Zhang, A. R. Arehart, H.-L. Huang, A. Genc, S. A. Ringel, C. G. Walle, D. A. Muller, and J. Hwang, Phys. Rev. X. **9**, 041027 (2019).
[55]S. Lany, APL Mater. **6**, 046103 (2018).
[56]S. Geller, J. Chem. Phys. **33**, 676–684 (1960).